Progress in Natural Science: Materials International 28 (2018) 430–436

HOSTED BY

Contents lists available at ScienceDirect

Progress in Natural Science: Materials International

journal homepage: www.elsevier.com/locate/pnsmi

Original Research

Transition-metal-doped Fe_2O_3 nanoparticles for oxygen evolution reaction

Yichun Yin[a], Xiwang Zhang[b], Chenghua Sun[c,*]

[a] ARC Centre of Excellence for Electromaterials Science, School of Chemistry, Monash University, Wellington Road, Clayton, VIC 3800, Australia
[b] Department of Chemical Engineering, Monash University, Wellington Road, Clayton, VIC 3800, Australia
[c] Faculty of Science, Engineering & Technology, Swinburne University of Technology, John St, Hawthorn, VIC 3122, Australia

ARTICLE INFO

Keywords:
Hematite
Metal doping
Water splitting
Oxygen evolution reaction

ABSTRACT

Hematite (α-Fe_2O_3) has been extensively studied as a promising photocatalyst, with the capacity to split water under visible light. To tune its electronic structure and improve the performance for oxygen evolution reaction (OER), high-quality single crystals of α-Fe_2O_3 nanoparticles were synthesized and doped by various transition metals (M = V, Cr, Mn, Zn, Co, Ni, Cu, Nb, Mo, Ti) by a molten-salt flux method. Optical, electronic and catalytic properties of transition-metal-doped α-Fe_2O_3 (TM-doped α-Fe_2O_3) have been systematically investigated. Cobalt has been identified as the best dopant for α-Fe_2O_3, reducing the OER overpotential by 0.16 V with respect to the undoped.

1. Introduction

Hematite (α-Fe_2O_3) is, in many aspects, a promising catalyst for oxygen evolution reaction (OER), which is the half reaction for solar water splitting photoelectrochemical (PEC) cells. Its main advantages include earth abundance, non-toxicity, chemical stability against photocorrosion in aqueous environment, and favorable band gap (2.0–2.2 eV, corresponding to absorption range of λ = 565–620 nm) [1]. Its absorption extends to the visible light range, which theoretically offers energy conversion efficiencies greater than 12% [2]. To date, however, various factors have limited the applications of hematite in photocatalytic water splitting, including large OER overpotential, poor conductivity and high electron-hole recombination rates, which attract extensive efforts to improve it, such as doping, morphology control and surface engineering.

Among various approaches, doping, typically through incorporating heteroatoms into the lattice, has been regarded to be an effective approach to improve the photocatalytic activity of metal oxides. Substitutional dopants can affect the electronic and photoelectrochemical properties by increasing the charge carrier density and thus the conductivity. For α-Fe_2O_3, numerous dopants have been employed to tune the catalytic performance for OER, including Si [3–7], Sn [8–12], Pt [13,14], Nb [15,16], Ni [17], Ti [6, 18–20], Al [18], Zn [15], Cr [21,22], Cd [23], Mo [22], and some have been proved to be effective. For instance, single Ti or Sn, and Be/Al co-dopants can increase the photocurrent response of Fe_2O_3 effectively [9]. To achieve effective doping, various methods have been developed, including electrodeposition [13], chemical deposition [8], dip coating [7], spin coating [11], spray pyrolysis [18], atmospheric pressure chemical vapour deposition (APCVD) [5]. Fe_2O_3 electrodes prepared by different methods often show wide difference in morphology and crystalline [3]; consequently, it is hard to compare the performance of the samples from different groups and establish a reliable understanding of the doping effect on the OER performance of hematite.

To achieve reliable comparison, all samples are synthesized by the same approach, ideally with dopants being incorporated into the lattice at the same time, which is helpful to control the dopants concentration and avoid the uncertainties in the following treatment. Molten-salt flux synthesis, which utilizes a mixture of eutectic salts as reactive medium, can be such an option. At the melting state, the mobility of ions is approximately 10^{10} times higher than the solid state [24] and thus, they can efficiently be incorporated to replace lattice atoms. In addition, defects associated with dopants can be removed under the high temperature. The reactants and subsequent products can be tailored by the salt mixture when the solubility of the product materials is less than the reactants. Molten salt method not only controls the morphology, but also tailors the doping level in a simple, cost-effective and scalable way. In this study, TM-doped Fe_2O_3 (M = V, Cr, Mn, Zn, Co, Ni, Cu, Nb, Mo, Ti) with high crystalline quality were fabricated by molten salt flux method. This offers us the opportunity to compare different dopants,

Peer review under responsibility of Chinese Materials Research Society.
* Corresponding author.
E-mail address: chenghuasun@swin.edu.au (C. Sun).

https://doi.org/10.1016/j.pnsc.2018.07.005
Received 17 March 2018; Received in revised form 25 July 2018; Accepted 25 July 2018
Available online 08 August 2018

from optical absorption to OER performance.

2. Experimental section

2.1. Preparation of Fe_2O_3 nanoparticles

Fe_2O_3 nanoparticles for TM-doping were fabricated by hydrothermal method. Aqueous solution contains 0.02 M $FeCl_3$ and 0.0003 M NaH_2PO_4 was carried out in a Teflon-lined autoclave at 100 °C for 48 h [25]. The precipitate was washed thoroughly by Milli-Q water and dried at 80 °C overnight in an oven.

2.2. Synthesis of TM-doped Fe_2O_3 nanoparticles

TM-doped Fe_2O_3 nanoparticles were synthesized by a molten salt flux method. Typically, 1 part (by weight) of as-prepared Fe_2O_3 nanoparticles, 1 part of Na_2HPO_4 and 4 parts of NaCl were ground with a mortar and a pestle to form a fine mixture. Then the mixture was transferred to a crucible with a lid and calcined inside a box furnace at 825 °C for 8 h. After calcination and cooling down to room temperature, the calcined products were washed in boiling Milli-Q water extensively to remove all soluble salts. The final products were dried at 80 °C overnight after three times centrifugal cleaning. The following chemicals were added (2% by atomic percentage) to fabricate TM-doped Fe_2O_3 nanoparticles: VCl_3, $K_2Cr_2O_7$, MnO_2, $ZnCl_2$, $CoCl_2{\cdot}6H_2O$, $NiCl_2{\cdot}6H_2O$, $Cu(NO_3)_2{\cdot}3H_2O$, Nb_2O_5, MoO_3, TiO_2.

2.3. Structural characterizations and electrochemical performance test

The morphology of TM-doped Fe_2O_3 nanoparticles were examined by a FEI Nova NanoSEM 450 field emission gun scanning electron microscope (FEGSEM). Transmission electron microscope (TEM) images and energy dispersive spectroscopy (EDS) mapping results were collected using a FEI Tecnai G2 F20 S-TWIN FEGTEM with an accelerating voltage of 200 kV and a Bruker energy dispersive X-ray (EDX) spectroscope. The X-ray diffraction (XRD) was recorded on a powder diffractometer (Bruker, D8, USA) using Cu Kα irradiation. The optical absorption spectra were recorded using a UV–vis scanning spectrophotometer (Shimadazu, UV-2600, Japan).

Electrochemical measurements were carried out using a CHI 660E workstation (CH Instruments, Inc., USA) in a three electrodes electrochemical cell, while Fe_2O_3 nanoparticles coated on fluorine doped tin oxide (FTO) glass substrate, a Pt plate and a KCl saturated Ag/AgCl electrode as the working, counter and reference electrodes, respectively. The working electrodes were prepared by dispersing 5 mg iron oxide in 1 ml 0.1% Nafion (Ethanol) thoroughly. Then 30 μl of the obtained mixed slurry was coated onto FTO glass and then the electrode was dried at 60 °C for 1 h. Liner sweep voltammetry test (LSV) was conducted at a scan rate of 50 mV/s in 1 M NaOH (pH = 13.6) purged with high purity N_2 gas. The current densities acquired from the LSV were normalized by the geometric surface area. The potential referenced to saturated Ag/AgCl reference electrode was converted into a reversible hydrogen electrode (RHE) potential using the formula:

$$E_{RHE} = E_{Ag/AgCl} + 0.059\text{pH} + E^0_{Ag/AgCl}$$

Where $E^0_{Ag/AgCl}$ is 0.1976 V at 25 °C, and $E_{Ag/AgCl}$ is the experimentally measured potential vs. the saturated Ag/AgCl electrode.

The Mott-Schottky analysis was accomplished to measure the charge transfer properties of TM-doped Fe_2O_3. The measurements were carried out by conducting an Impedance-Potential spectroscopy at 500 Hz by scanning the potential from −1.0–0 V in a step of 10 mV/s. Charge carrier density (N_d) and flat band potential (E_{fb}) were calculated using the following equation:

$$\frac{1}{C_{SC}^2} = \frac{2}{\varepsilon\varepsilon_0 e N_d}\left(\text{E} - \text{Efb} - \frac{kT}{e}\right)$$

where C_{sc} is the space charge region capacitance per unit area, ε is the dielectric constant of iron oxide (ε = 14.2 F/m in this study), ε_o is the vacuum permittivity, e is the electron charge, N_d is the charge carrier density, k is the Boltzmann's constant, and T is the temperature (K). The position of conductive band (CB) could be approximated by the flat band potential (E_{fb}) [26]. Milli-Q water was used for preparing the solutions. All the measurements were performed at room temperature.

3. Results and discussion

3.1. Structures of undoped and TM-doped Fe_2O_3 nanoparticles

The presentative SEM images of the as-prepared α-Fe_2O_3 nanoparticles and TM-doped α-Fe_2O_3 nanoparticles are shown in Fig. 1. The starting α-Fe_2O_3 material for TM-doping synthesized by hydrothermal method are spin-shaped nanoparticles, which is about 400 nm in length and 100 nm in width. TM-doped samples through molten salt flux method are all truncated-dodecahedron shaped particles about 100–200 nm in diameter, which could exclude the different morphology effect on OER.

XRD patterns (Fig. 2) shows that the non-doped Fe_2O_3 and TM-doped Fe_2O_3 are well indexed to the diffraction peaks of α-Fe_2O_3 crystalline phase (space group: *R3c* (167), a = 0.5036, b = 0.5036, c = 1.3749, JCPDS 33–0664). In addition, metal dopants did not exist as solid or metal oxides. However, several diffraction peaks with low intensity are appeared in the doped samples through molten salt flux method compared with the as-prepared α-Fe_2O_3 nanoparticles, which is unclear and is subject of further investigation.

TEM images and corresponding selected area electron diffraction (SAED) pattern of Co-doped Fe_2O_3 are shown in Fig. 3(a–d). The lattice fringes in high resolution transmission electron microscope (HRTEM) image are with spacing of 0.25 nm and angles of 60°, which are well indexed to the (11 − 20) lattice spacing of the rhombohedral hematite (Fig. 3(c)). The corresponding SAED pattern from [0001] zone axis (Fig. 3(d)) further confirms the single crystalline nature of the sample with hexagonal spot pattern. The top and bottom surfaces of the rhombohedral Co-doped α-Fe_2O_3 are ascribed to (0001) and (000 − 1) planes, respectively. As the incident electron beam was projected along the [0001] direction, the spots are directed to (-2110), (-1-120), (1-210), (2-1-10), (11-20), (-12-10) planes as the side surfaces.

Energy dispersive X-ray spectroscopy (EDS) mapping was also carried out to identify the chemical composition of Co-doped Fe_2O_3 nanoparticles (Fig. 4(a–f)). Fig. 4(a–b) show bright-field (BF) image and high-angle annular dark-field (HADDF) image of a single nanoparticle of Co-doped Fe_2O_3. The EDS mapping results indicate that the Co dopants are uniformly distributed with an atom percentage about 1.8%. The result shows small trace of phosphorus with atoms ratio far below the Co dopants (Fig. 4(f)). We presume this is related to the new peaks with low intensity. To exclude the effect of phosphorus on OER, a non-doped sample using the same procedure was prepared, the electrochemical performance does not change with the small amount of phosphorus residual comparing with the starting material.

3.2. Optical absorption and band gap

TM dopants, which may create additional states, have been explored

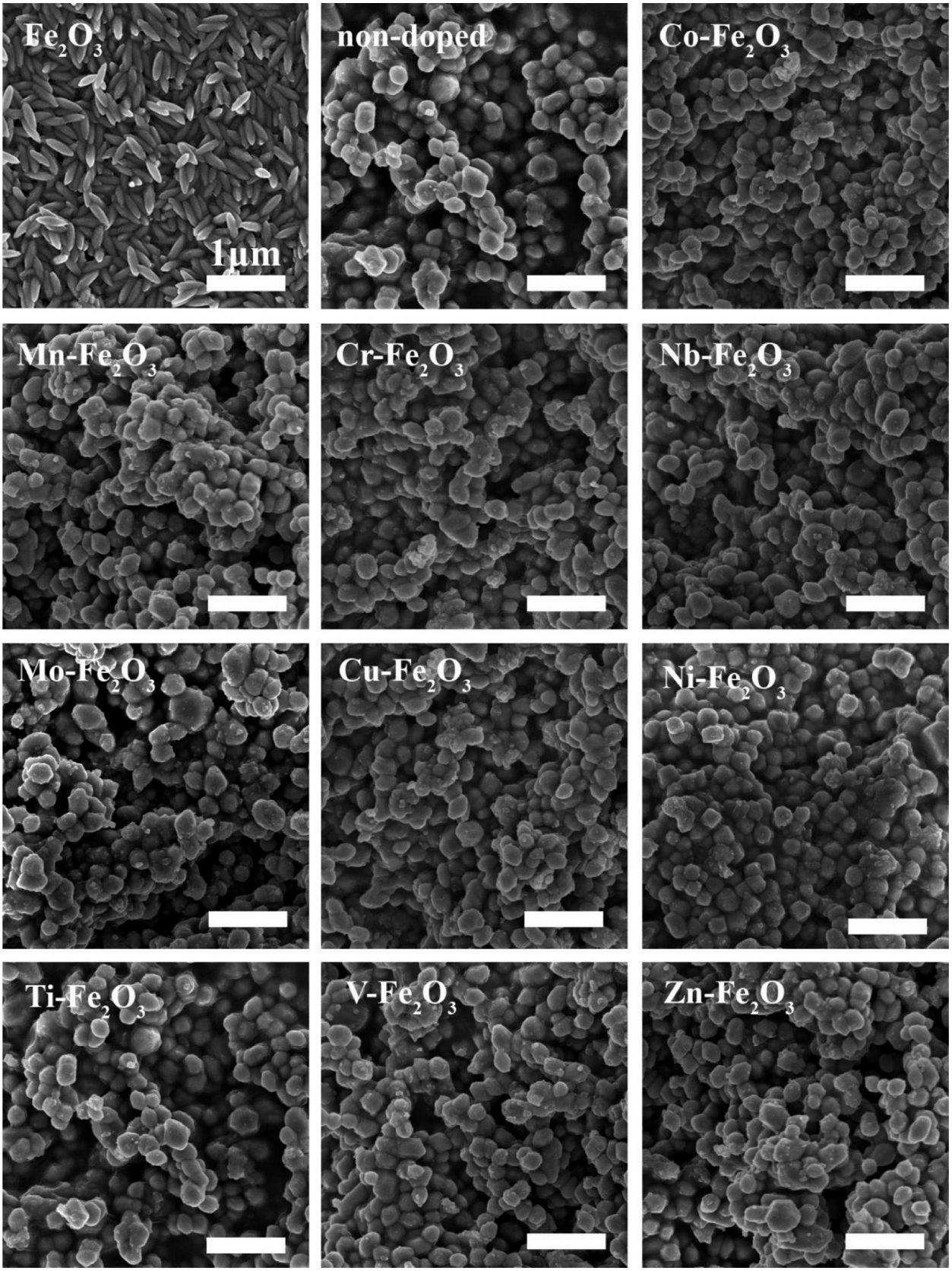

Fig. 1. SEM images of the as-prepared, non-doped and TM-doped Fe_2O_3 nanoparticles.

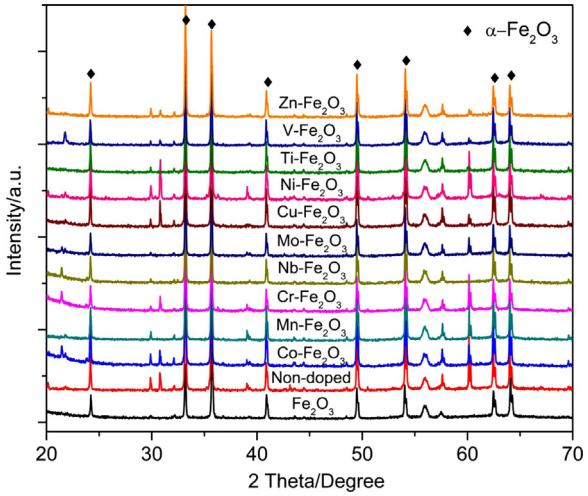

Fig. 2. XRD patterns of as-prepared Fe_2O_3 nanoparticles, non-doped and TM-doped Fe_2O_3 nanoparticles.

to modify the electronic structure of metal oxides, based on which the light absorption and the reactivity under visible light can be understood. Fig. 5(a) shows the UV–vis absorbance spectra of non-doped and TM-doped Fe_2O_3 nanoparticles. The Tauc plots for both direct and indirect transitions are shown in Fig. 5(b–c) and the band gap energy is given in Table 1. Here, Fe_2O_3 showed broad absorption in the investigated wavelength range. The direct and indirect bandgaps are about 2.0 eV. The bandgap of Fe_2O_3 is slightly reduced by most TM-doping, leading to better visible light absorption. Mn-doping shows the narrowest band gap. These values are matched well with previously reported literature of hematite (1.9–2.2 eV [27,28]).

Transition metals are cation substitutions to Fe atoms,which either have smaller or bigger ionic radius than host Fe atoms. The differences of ionic radius would results in differences of coupling between the nearby atoms and therefore, are likely to increase the photo response [29]. As for electronic structures, the coupling interaction effect between the substitutional transition metal dopants and host Fe atoms would create additional density states in the bandgap of Fe_2O_3, and subsequently move the conductive band minimum upward closer to the H_2O/H_2 redox level. Since Fe_2O_3 is already a good absorbor of visible light, the incorporation of substitutional transition metal dopants could only slightly reduce the bandgap of Fe_2O_3 under this circumstance.

3.3. Electrochemical and charge transport properties

Fig. 6(a) shows LSV plots of TM-doped Fe_2O_3 electrodes. The incorporation of TM atoms into the Fe_2O_3 lattice result in various decreases of overpotential, while the overpotential η for OER is determined at $I = 0.5\,mA/cm^2$ and listed in Table 1. The listed data testified that TM dopants can improve the catalytic activity of Fe_2O_3 and cobalt is the most effective candidate (reduce η by 0.16 V), which agrees with DFT calculations prediction [30].

In this study, the flatband potential (E_{fb}) of un-doped and TM-doped Fe_2O_3 is around $-0.5\,V \sim -0.6\,V$ versus NHE and the charge carrier density calculated from the slopes of the Mott−Schottky plots (Fig. 6(b)) are in the range of $9.46 \times 10^{19} \sim 3.85 \times 10^{20}\ cm^{-3}$. The

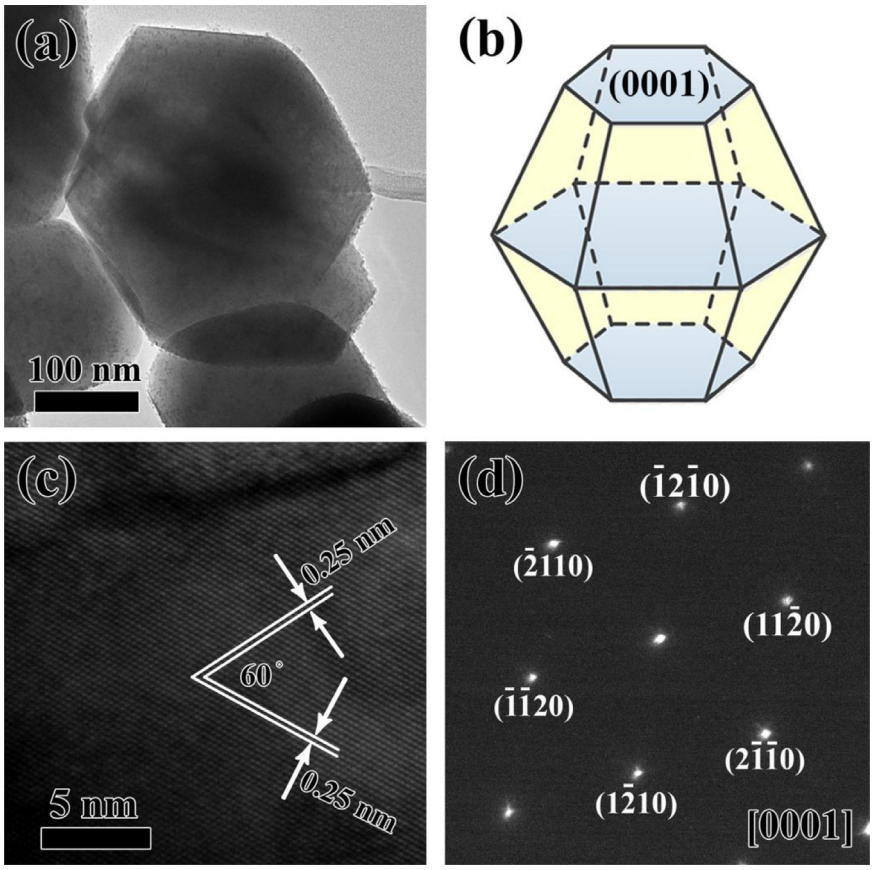

Fig. 3. (a) TEM image, (b) schematic drawing, (c) HRTEM image and (d) corresponding selected area diffraction pattern (SAED) of Co-doped Fe_2O_3 nanoparticles.

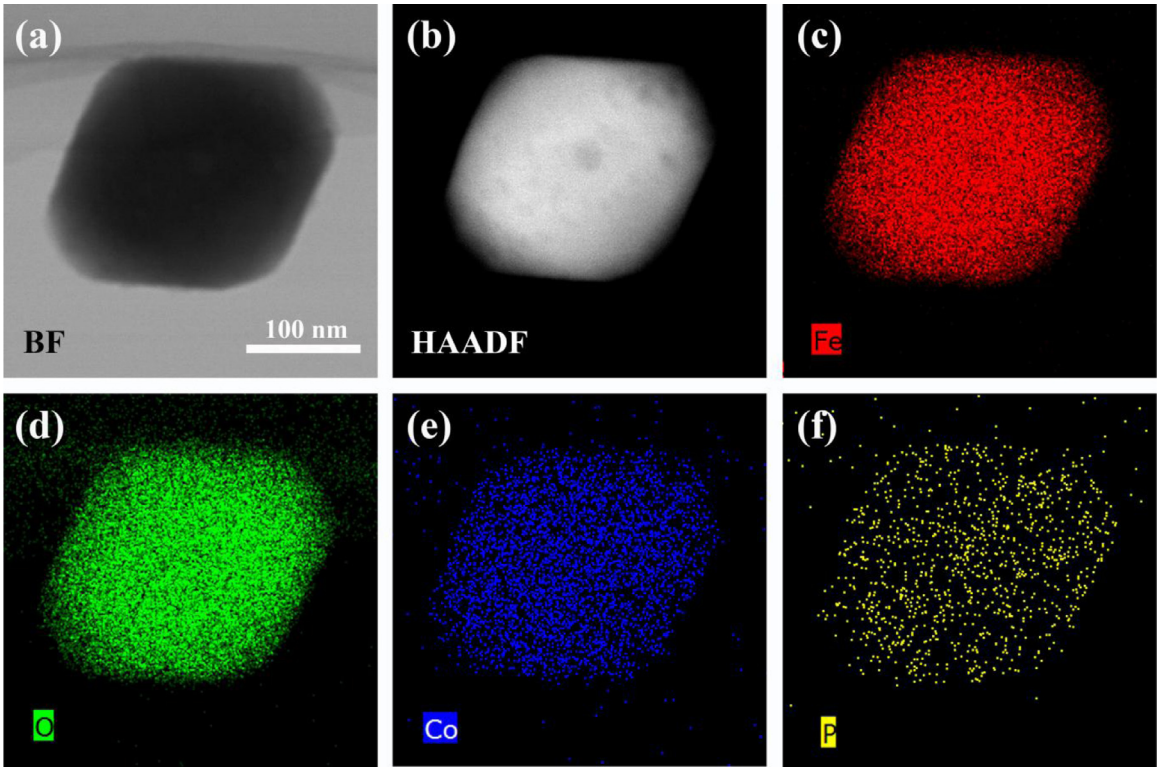

Fig. 4. (a) Bright field (BF), (b) high-angle annular dark field (HAADF) images and (c-f) EDS elemental mapping of Co-doped Fe_2O_3 nanoparticles.

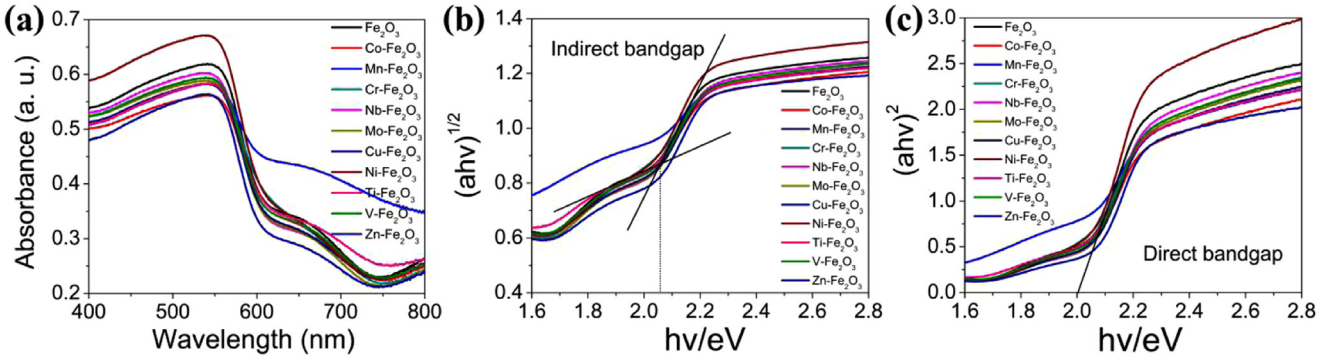

Fig. 5. (a) UV–vis spectra; (b) indirect and (c) direct transitions: $(\alpha h\nu)^{1/2}$ and $(\alpha h\nu)^2$ vs. $(h\nu)$ of non-doped and TM-doped Fe_2O_3.

calculated charge carrier density (N_d) and flatband potential (E_{fb}) are summarized in Table 1. The increases of charge carrier density indicates that almost all the transition metals are successfully incorporated into hematite and act as ionized donors and therefore, improve the electrical conductivity. The positive slope indicates n-type behaviour of non-doped and TM-doped Fe_2O_3 nanoparticles. The negative shift of E_{fb} also reveals that doped Fe_2O_3 is n-type and the dopants are incorporated at the Fe^{3+} sites [9].

The overpotential for OER is depending on two aspects: the conductivity for electrons and holes to transport, and the thermodynamic kinetics for the four elementary steps of OER:

$$* + H_2O \rightarrow *OH + H^+ + e^- \quad (1)$$

$$*OH \rightarrow *O + H^+ + e^- \quad (2)$$

$$*O + H_2O \rightarrow *OOH + H^+ + e^- \quad (3)$$

$$*OOH + H_2O \rightarrow O_2 + H^+ + e^- \quad (4)$$

Where * represents the catalyst surface, and *O, *OH and *OOH are the intermediate states associated with OER. Each elementary reaction

Table 1
Experimental OER overpotential, bandgap, charge carrier density (N_d) and flat band potential (E_{fb}) of TM-Doped Fe_2O_3 in 1 M NaOH. The reported theoretical OER overpotential for TM-Doped hematite single crystal from DFT calculation are listed for comparison.

Sample 2% dopant	Overpotential (V) vs. RHE		Bandgap (eV)		N_d (cm^{-3})	E_{fb} (V) vs. NHE
	Exptl, at 0.5 mA/cm^2	cald [29]	Indirect	Direct		
Fe_2O_3	0.50	0.77	2.06	2.02	1.27×10^{20}	− 0.48
Co-Fe_2O_3	0.34	0.71	2.05	1.99	1.70×10^{20}	− 0.54
Mn-Fe_2O_3	0.39	1.46	2.08	1.91	2.48×10^{20}	− 0.61
Cr-Fe_2O_3	0.43		2.05	1.97	1.96×10^{20}	− 0.52
Nb-Fe_2O_3	0.43		2.04	2.02	1.91×10^{20}	− 0.51
Mo-Fe_2O_3	0.43		2.05	2.01	3.85×10^{20}	− 0.51
Cu-Fe_2O_3	0.44		2.05	1.99	1.34×10^{20}	− 0.50
Ni-Fe_2O_3	0.37	0.64	2.05	2.02	9.46×10^{19}	− 0.50
Ti-Fe_2O_3	0.43	2.21	2.06	2.00	1.97×10^{20}	− 0.51
V-Fe_2O_3	0.45		2.06	2.01	2.46×10^{20}	− 0.52
Zn-Fe_2O_3	0.47		2.08	2.01	2.77×10^{20}	− 0.62

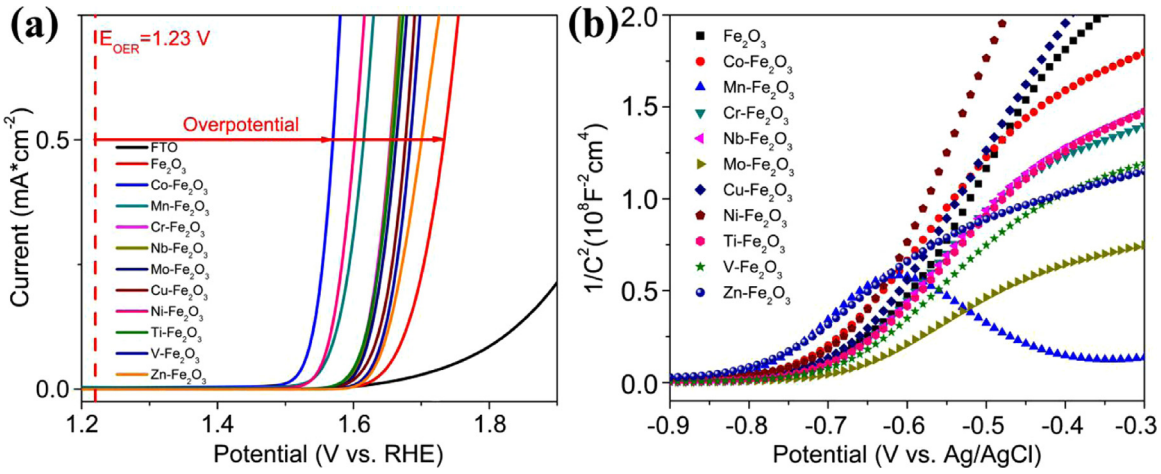

Fig. 6. (a) Overpotential measurements of FTO and Fe_2O_3 with/without TM-doping electrodes, dashed vertical red lines represent the thermodynamic redox potential for OER at pH ~13.6; (b) Mott-Schottky plots were measured at 500 Hz.

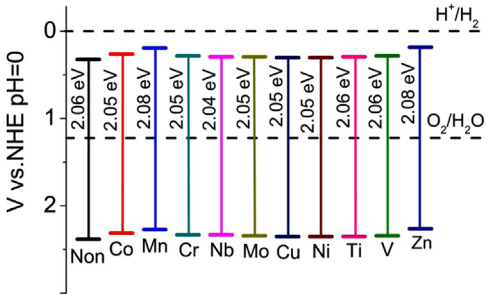

Fig. 7. Comparative VBM (up limit) and CBM (down limit) of Fe_2O_3 and TM-doped Fe_2O_3 in aqueous solution at pH = 0.

needs an energy over the standard potential of water oxidation 1.23 eV. The highest extra energy of the four steps is referred to overpotential. The dopants on the surface are likely to serve as the reactive sites for OER, and the dopants farther under the surface would mainly improve the charge carrier transport. Since all the transition metals can increase the charge carrier density, which improve the conductivity, by around 1 ~ 3 times. The crucial aspect is the surface reaction kinetics.

The rate determining steps require hole localization on the active oxygen atoms of the surface. Co and Ni have less positive charges between + 2 and + 3 when electrons are being added or removed, offer the smaller binding energies of reaction intermediates. According to Carter's calculation work that cobalt and nikle doped Fe_2O_3 have the most favorable thermodynamic OER reaction pathways and offer the lower overpotentials than other dopants, which are consistent with our experimental results.

It is interesting to notice that Ni doping can effectively reduce the overpotential for OER (by ~0.13 V), but the calculated charge carrier density is slightly lower than the undoped Fe_2O_3. On the contrary, Zn dopant enhanced the N_d by more than twice with a small overpotential reduce of 0.03 V. This could be explained by Liao et al.'s work [30] that Ni dopants in α-Fe_2O_3 can modulate and balance the binding strengths of water oxidation intermediates on the reactive surfaces, which improves the OER reaction thermodynamics on Ni-doped Fe_2O_3. In addition, their DFT calculation work are based on (0001) surface. The exposed surfaces play an important role in catalytic performance. Taking into spatial charge separation into account, the catalytic activity of side crystal surfaces {0112} are higher than the {0001} surface [31,32]. And the Fe_2O_3 electrodes are complex with facets, vacancies and hydroxylation, all these factors can result in the difference between experimental data and DFT calculation.

Based on the measured flatband potential, the valence band maximum (VBM) and conductive band minimum (CBM) have been listed in Fig. 7 for comparison, from which it is clearly that TM dopants can impact slightly on both the VBM and CBM, and in the cases of Co, Mn, Cr, Zn-doping, band edges are shifted upward, indicating that the observed reduce of the overpotential is not only due to the kinetics improvement, but also the driving force for hole transfer from VB to water actually becomes smaller.

4. Conclusions

The effect of transition metal doping on the optical absorption and electrochemical properties of Fe_2O_3 has been systematically studied using ten dopants (V, Cr, Mn, Zn, Co, Ni, Cu, Nb, Mo, Ti). It is found that: (1) these dopants can only slightly change the band gap (0.1 eV or less for both direct and indirect band gap), among these metals Mn is the most efficient dopant to improve the visible light absorption; (2) both CBM and VBM of Fe_2O_3 can be slightly shifted; (3) Almost all the TM dopants can increase the charge carrier density and thus, improve the electrical conductivity of Fe_2O_3, cobalt is the most efficient candidate to reduce the OER overpotential (by 0.16 V).

Acknowledgements

The authors acknowledge the Australian Research Council (ARC) for the support through the Excellence for Electromaterials Science (ACES) and Future Fellowship (CS, FT130100076). We also acknowledge the use of facilities within the Monash Centre for Electron Microscopy (MCEM), ARC funding (LE110100223) and the Monash X-ray Platform.

References

[1] K. Sivula, F. Le Formal, M. Grätzel, ChemSusChem 4 (2011) 432–449.
[2] A.B. Murphy, P.R.F. Barnes, L.K. Randeniya, I.C. Plumb, I.E. Grey, M.D. Horne, J.A. Glasscock, Int. J. Hydrog. Energy 31 (2006) 1999–2017.
[3] I. Cesar, A. Kay, J.A.G. Martinez, M. Grätzel, J. Am. Chem. Soc. 128 (2006) 4582–4583.
[4] X. Wang, K.Q. Peng, Y. Hu, F.Q. Zhang, B. Hu, L. Li, M. Wang, X.M. Meng, S.T. Lee, Nano Lett. 14 (2014) 18–23.
[5] A. Kay, I. Cesar, M. Grätzel, J. Am. Chem. Soc. 128 (2006) 15714–15721.
[6] M. Rahman, N. Wadnerkar, N.J. English, J.M.D. MacElroy, Chem. Phys. Lett. 592 (2014) 242–246.
[7] Y. Hu, D.K. Bora, F. Boudoire, F. Häussler, M. Grätzel, E.C. Constable, A. Braun, J. Renew. Sustain. Energy 5 (2013) 043109.
[8] S. Park, H.J. Kim, C.W. Lee, H.J. Song, S.S. Shin, S.W. Seo, H.K. Park, S. Lee, D.W. Kimb, K.S. Hong, Int. J. Hydrog. Energy 39 (2014) 16459–16467.
[9] J.S. Jang, J. Lee, H. Ye, F.R.F. Fan, A.J. Bard, J. Phys. Chem. C 113 (2009) 6719–6724.
[10] L. Xi, S.Y. Chiam, W.F. Mak, P.D. Tran, J. Barber, S.C.J. Loo, L.H. Wong, Chem. Sci. 4 (2013) 164–169.
[11] J. Frydrych, L. Machala, J. Tucek, K. Siskova, J. Filip, J. Pechousek, K. Safarova,

M. Vondracek, J.H. Seo, O. Schneeweiss, M. Grätzel, K. Sivula, R. Zboril, J. Mater. Chem. 22 (2012) 23232.
[12] J.S. Jang, K.Y. Yoon, X. Xiao, F.R.F. Fan, A.J. Bard, Chem. Mater. 21 (2009) 4803–4810.
[13] Y.S. Hu, A. Kleiman-Shwarsctein, A.J. Forman, D. Hazen, J.N. Park, E.W. McFarland, Chem. Mater. 20 (2008) 3803–3805.
[14] H.G. Cha, J. Song, H.S. Kim, W. Shin, K.B. Yoon, Y.S. Kang, Chem. Comm. 47 (2011) 2441–2443.
[15] V.M. Aroutiounian, V.M. Arakelyan, G.E. Shahnazaryan, G.M. Stepanyan, E.A. Khachaturyan, H. Wang, J.A. Turner, Sol. Energy 80 (2006) 1098–1111.
[16] C. Sanchez, K.D. Sieber, G.A. Somorjai, J. Electroanal. Chem. 252 (1988) 269–290.
[17] Y. Liu, Y.X. Yu, W.D. Zhang, Electrochim. Acta 59 (2012) 121–127.
[18] C.J. Sartoretti, B.D. Alexander, R. Solarska, I.A. Rutkowska, J. Augustynski, J. Phys. Chem. B 109 (2005) 13685–13692.
[19] J. Engel, H.L. Tuller, Phys. Chem. Chem. Phys. 16 (2014) 11374–11380.
[20] H. Magnan, D. Stanescu, M. Rioult, E. Fonda, A. Barbier, Appl. Phys. Lett. 101 (2012) 133908.
[21] A. Boudjemaa, M. Trari, Int. J. Hydrog. Energy 35 (2010) 7684–7689.
[22] A. Kleiman-Shwarsctein, Y.S. Hu, A.J. Forman, G.D. Stucky, E.W. McFarland, J. Phys. Chem. C 112 (2008) 15900–15907.
[23] A. Bak, W. Choi, H. Park, Appl. Catal. B: Environ. 110 (2011) 207–215.
[24] R.H. Arendt, J.H. Rosolowski, J.W. Szymaszek, Mater. Res. Bull. 14 (1979) 703–709.
[25] T. Sugimoto, A. Muramatsu, K. Sakata, D. Shindo, J. Colloid Interface Sci. 158 (1993) 420–428.
[26] M.A. Alpuche-Aviles, Y. Wu, J. Am. Chem. Soc. 131 (2009) 3216–3224.
[27] K. Sivula, R. Zboril, F.L. Formal, R. Robert, A. Weidenkaff, J. Tucek, J. Frydrych, M. Grätzel, J. Am. Chem. Soc. 132 (2010) 7436–7444.
[28] P.B.I. Herrmann-Geppert, L. Hepperle, S. Fiechter, ECS Trans. 41 (2012) 201–212.
[29] H. Magnan, D. Stanescu, M. Rioult, E. Fonda, A. Barbier, Appl. Phys. Lett. 101 (2012) 133908.
[30] P. Liao, J.A. Keith, E.A. Carter, J. Am. Chem. Soc. 134 (2012) 13296–13309.
[31] J.Y.T. Chan, S.Y. Ang, E.Y. Ye, M. Sullivan, J. Zhang, M. Lin, Phys. Chem. Chem. Phys. 17 (2015) 25333–25341.
[32] Y. Zhao, F. Pan, H. Li, T. Niu, G. Xua, W. Chen, J. Mater. Chem. A 1 (2013) 7242–7246.